AN ELECTROLYTIC-INDUCED BUBBLE-BASED DISSOLVED CO_2 SENSOR

Steven Tran, Seungbeom Noh, and Hanseup Kim*
Electrical and Computer Engineering, University of Utah, Salt Lake City, UT, USA

ABSTRACT

This paper presents the first integrated bubble-based gas sensor that quantifies dissolved CO_2 in aquatic environments by integrating a microcavity electrode tip for nucleation control, an electromagnetic flow system for passive bubble transportation and an interdigitated capacitive sensor for compact and low power sensing. Previously we proved that there exists a correlation between bubble size which was optically measured in relation to the gaseous CO_2 concentration surrounding the water. Here we realized the first proof-of-concept microfabricated sensor, with the ability for on-chip bubble measurement, such that it can be utilized within an aquatic environment. The fabricated bubble-based sensor demonstrated (1) a precise control of the bubble nucleation location with approximately 6.88 times greater precision and yielding an average reference bubble size forming within 1.5 µm radius of the theoretical value, (2) an efficient detachment and transportation of a bubble to a sensing zone within 5 seconds, and (3) a sensitivity of 0.03 nF·ppm^{-1} with a resolution of 3 ppm for CO_2 detection. These features will help facilitate the future deployment of a dissolved CO_2 bubble-based sensor for in-situ sensing within aquatic environments.

INTRODUCTION

Amidst worsening global climate conditions, carbon sequestration emerges as a pivotal strategy to combat climate change, with the aim of achieving net-zero carbon emissions by 2100, as stipulated by the Intergovernmental Panel on Climate Change [1]. Among carbon sequestration methods, ocean-based carbon sequestration holds promise due to its expansive surface area and high-pressure environment conducive for effective carbon storage [2]. However, its optimization and scaling have been hindered by inadequate sensing capabilities, notably the absence of a non-degradable, real-time, in-situ dissolved CO_2 measurements, crucial for feedback systems to optimize oceanic carbon sequestration in response to dynamic CO_2 fluxes within the ocean.

To enable the required non-degradable, real-time, in-situ aquatic CO_2 sensing capability, the use of a bubble as a sensing modality was previously suggested and verified [3]. Although previous studies demonstrated a consistent correlation between bubble size and CO_2 concentration, suggesting the feasibility of bubble-based sensing, this concept had not yet been implemented into an integrated microsensor system.

This paper presents the operational principle, three key design elements, microfabrication process, and testing outcomes of the pioneering integrated bubble-based gas sensor tailored for assessing aquatic CO_2 concentrations, with the incorporation of a microcavity electrode tip for controlled bubble nucleation, an electromagnetic flow system for rapid bubble transportation, and an interdigitated capacitive sensor, replacing the traditional optical methods for a more compact, low-power bubble size measuring system.

OPERATION PRINCIPLE

The 25 × 25 × 4 mm^3 proposed sensor functions by submerging it in water to fill the 25 mL microchannel. Upon application of an electrolytic voltage of 3.7 V for 10 seconds generating a current of 57 µA (energy consumption: 2 mJ) at the bubble nucleating electrode, water molecules around the electrode decompose into H_2 and O_2 gases. These gases nucleate bubbles at the anode and cathode tips, establishing an initial reference bubble size. Subsequently, these reference bubbles are transported to the interdigital capacitive sensor to monitor the changes in size, facilitated by a buoyancy and electromagnetic forces (Fig. 1-Stage 1). The electromagnetic force, activated during bubble nucleation period, enhances bubble flow from 0.10 mm·s^{-1} to 0.44 mm·s^{-1} through the utilization of a magnet with a magnetic flux density of 195 mT.

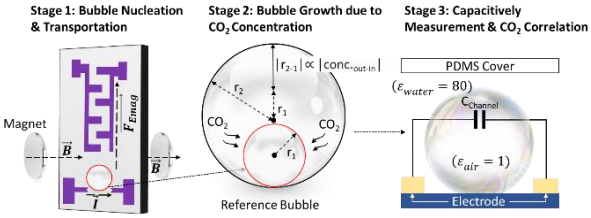

Fig 1. The operational principle of the electrolytic-induced bubble-based CO_2 sensor composing of three primary stages.

Over time, bubble size increases proportionally with the dissolved CO_2 concentration due to its high solubility and rapid mass transfer rate, a phenomenon described by Epstein-Plesset's as shown in Eq. 1 where, R represents the bubble radius at time t, k is the diffusion coefficient of the gas into liquid, ρ denotes the gas density, C_i is the initial gas concentration in the bubble, and C_s indicates the gas concentration within the solution. (Fig. 1-Stage 2).

$$\frac{dR}{dt} \propto k\frac{C_s}{\rho}\left(1-\frac{C_i}{C_s}\right)\left(\frac{1}{R}+\frac{1}{\sqrt{\pi kt}}\right) \quad (1)$$

Assuming that the time-dependent component remains constant and C_i is close to zero, a bubble growth constant can be established for comparison of various gases, as shown in Table 2 using Eq. 2.

$$\textbf{Bubble Growth Constant} = \frac{k(C_s)}{\rho} \quad (2)$$

When analyzing the bubble growth constant for the typical gas composition of ocean water, it becomes evident that CO_2 plays a significant role in the majority of the growth, contributing approximately 93% compared to other gases.

978-1-940470-05-4/HH2024/$25©2024TRF
DOI 10.31438/TRF.HH2024.14

Table 2: Table summarizing the gas found in the ocean and their effects on the growth of a bubble.

Gases	% in Atmosphere	Solubility (g/kg of water)	% in Ocean	~Concentration in Ocean (ppm)	Diffusion Coefficient ($x10^{-5}$ cm^2/s)	Bubble Growth Constant	Growth Rate Composition %
CO_2	0.043	2.67	83	424	6.35	2.108	93.52
N_2	78.08	0.025	11	56	2.00	0.088	3.91
O_2	20.95	0.057	6	31	2.42	0.058	2.57
Ar	0.93	0.08	0	0	2.50	0	0
Ne	0.0018	0.0082	0	0	3.64	0	0
He	0.00052	0.0016	0	0	7.28	0	0
CH_4	0.0002	0.033	0	0	1.84	0	0

The bubble size was then measured capacitively using an integrated interdigital electrode, allowing for compact, low-power in-situ measurements (Fig. 1-stage 3). The interdigital electrode, with a width of 200 µm, length of 300 µm, and pitch of 300 µm, ensures that a 1 µm change in bubble radius corresponds to a 0.1 nF change in capacitance. Utilizing these parameters, the capacitance was quantified based on the difference in permittivity between the bubble and water, as per Eq. 3,

$$C = \frac{2(Rx*\varepsilon_{air}+(1-Rx)*\varepsilon_{water})\varepsilon_0}{\pi} ln\left[\left(1+\frac{w}{a}\right)+\sqrt{\left(1+\frac{w}{a}\right)^2-1}\right] \quad (3)$$

where R_x represents the ratio of the air bubble to water across the capacitive sensor, w denotes the interdigital capacitive width, and a indicates the interdigital capacitive pitch. As a result, as the bubble size increases, the capacitance decreases due to the lower permittivity coefficient of the air bubble. Further optimization of the capacitive sensor parameters is expected to enhance sensor resolution, pending additional characterization of the bubble and its temporal size changes.

DEVICE PROTOTYPING

Microfabrication

The 25 × 25 × 4 mm^3 dissolved CO_2 sensor features microfabricated platinum electrodes on a glass substrate, bonded with a 25 mL PDMS-based microchannel.

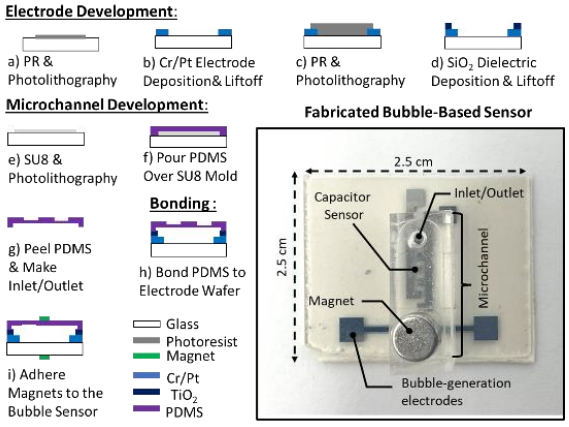

Fig 2. Process flow of bubble sensor and an image of a completed fabricated device.

Fabrication details are shown in Figure 2 which further elaborated upon in prior work [3]. Notably, novel design elements including a 10 µm radius cavity structure and a 50 nm thick TiO_2 passivation layer was deposited across the bubble nucleation electrodes. These additions aim to enhance precision in bubble nucleation by reducing surface energy, promoting gas accumulation and bubble formation within the microcavity, while isolating conductive areas to just the tip of the electrode, ensuring exclusive nucleation at the cavity for improved gas accumulation. Additionally, two neodymium magnets, with a magnetic flux density of 195 mT, were attached to the sensor. This generates an electromagnetic force, aiding bubble transportation to the capacitive sensor without any added power during the bubble generation period.

TEST METHODOLOGY

Location and Size Control in Bubble Nucleation

To assess the repeatability of bubble formation at specific locations, the distance between the center of mass of the produced bubbles at the tip of the cavity was measured across 12 trials for each of the two comparison devices. One device featured the nucleation cavity at the tip and a TiO_2 passivation layer covering the whole electrode except for the tip. The other device, representing the previous version [3], did not contain those features. To initiate bubble formation, a 3.7 V voltage was applied for 10 seconds in each test. Subsequently, the distance between the center of the nucleated bubble and the tip of the cavity was promptly captured using a digital microscope (VHX-5000, Keyence). From the captured image, the average distance was then calculated and compared for each of the two devices. Note that a 25 um x 75 um section of the electrode tip was observed for a relatively fair comparison.

Additionally, the repeatability of controlling bubble size was evaluated by quantifying the transient size changes of a bubble's radius over a 5-minute interval across four trials, employing the same bubble nucleation conditions described earlier The transient size changes were monitored once a bubble entered the interdigitated capacitive sensor zone The bubble's radius was then optically measured at four time-points (0.5, 1, 2, and 5 minutes) using the VHX-5000 microscope by Keyence, with the average deviation from the bubble's mean radius calculated for each time point. This was then averaged across all the time point to calculate the average absolute deviation of the reference bubble size and its standard deviation. Note that all the testing was performed with a dissolved CO_2 value of 0.62 ppm.

Magnetic Flux Density Optimization

To validate and optimize the magnetic-field-assisted transportation of a bubble from the nucleation electrode to the integrated capacitive sensing electrode, microbubbles produced in the microfabricated sensor were exposed to various magnetic flux densities ranging from 0 to 200 mT, while their transit time through the capacitive sensor was quantified. Once a bubble was nucleated at the tip of an electrode, it detached from the electrode passively due to the buoyancy force and was transported to the capacitive sensing electrode. To expedite transportation, magnets could be included to induce a Lorentz' force on the dipole water-based bubble, supplementing the passive buoyancy force. The bubble transient time was measured by monitoring the capacitance transition period between from $pF \cdot s^{-1}$ to $nF \cdot s^{-1}$, using a multimeter (Fluke-117, Fluke). Note that the magnetic flux was varied gradually using neodymium

magnets centered around the bubble generating electrode, with the magnetic flux density measured using a WT10A tesla meter.

Capacitive CO_2 Bubble Measurements

To validate the effectiveness of the capacitive measurements for the bubble size and CO_2 concentrations within the surrounding water, the microfabricated sensor equipped with an interdigitated capacitive sensor was submerged in water with dissolved CO_2 concentrations ranging from 0.62 to 987.36 ppm, while monitoring the size of the produced bubbles both capacitively (Fluke-117, Fluke) and optically (VHX-5000, Keyence) across 3 trials for each of the tested dissolved CO_2 concentration. The CO_2 pressure was adjusted to four concentrations of 0.62, 98.74, 246.84, and 987.36 ppm by manipulating the CO_2 pressure in a chamber that contained water with the immersed sensor. Note, that the CO_2 pressure was set to 4.14×10^{-4}, 6.59×10^{-2}, 1.65×10^{-1}, and 6.60×10^{-1} ATM, respectively, which, utilizing Henry's law (Eq. 4), produced the respective four concentrations used for the testing.

$$\boldsymbol{C = kP} \tag{4}$$

In the equation, C is the dissolved gas concentration, k is Henry's constant for CO_2 (1496.34 ppm·ATM^{-1}) and P is the partial pressure of CO_2. Note that the optical measurements and the capacitance measurements were then plotted against the CO_2 concentrations for correlation.

RESULTS

Fixed Point Bubble Nucleation and Reduced Bubble Size Deviation Using a Micro Cavity

The integration of electrode design features, including the microcavity tips and the TiO_2 passivation layer, successfully demonstrated repeatable bubble nucleation at the targeted locations with ~6.88 times less deviation in distance as compared to the device without the additional design features, as shown in Fig. 3. We believe that the incorporation of a microcavity at the electrode tip reduces the surface energy thereby reducing the energy needed for bubble nucleation, thus allowing the preferred gas to accumulate and form bubbles. The incorporation of passivation TiO_2 also effectively isolated all other conductive areas of the electrode in contact with water, preventing electrolytic reactions at the passivized location.

Moreover, transient bubble size measurements revealed a progressive increase in bubble size over time with an average standard deviation of approximately 20.1% over the 4 observed measurement time (Fig. 4). While this deviation is relatively high, it signifies a notable improvement of 40.2% compared to the previous design. It is notable that the theoretical estimation of the bubble detachment radius, calculated as 123 µm using Fritz's formula in Eq. 5 with a cavity radius of 10 µm and an approximate bubble contact angle of 10 degrees, closely matched the measured average radius of the bubbles produced, which was 124.5 µm at 0.5 minutes. However, an average deviation of 32.4 µm persisted. This average deviation arises from the reference bubble experiencing higher-than-expected stiction at the electrode, encountering surface tension not only at the electrode but also at the substrate. With an electrode thickness of 400 nm and a generated bubble radius exceeding 100 µm, the bubble immediately comes in contacts with the substrate surface, a factor not considered in Fritz's formula, compromising the precision of the detachment radius. To address this issue in the future, a trench-based design will be etched from the substrate, eliminating stiction between the substrate and the bubble and enabling bubble nucleation and detachment to better adhere to Fritz's formula.

$$\boldsymbol{r_d = \sqrt[3]{\frac{3r_c\sigma sin(\theta)}{2\Delta\rho g}}} \tag{5}$$

In Eq. 5, the theoretical radius at which the bubble detaches (r_d) can be computed based on the cavity radius (r_c), surface tension (σ), bubble contact angle (θ), density (ρ), and gravitational constant (g) [5].

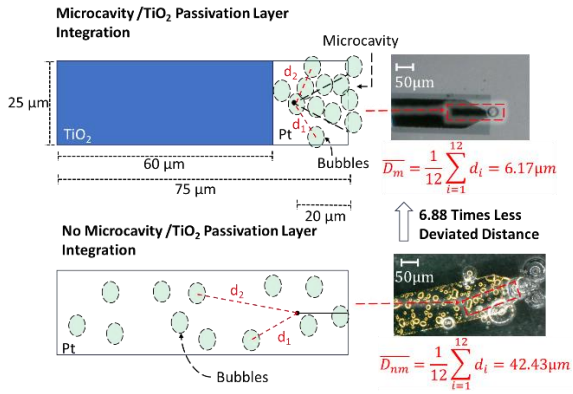

Figure 3: Bubble location control testing of two device where one device has an integrated TiO_2 passivation and a microcavity and the other does not.

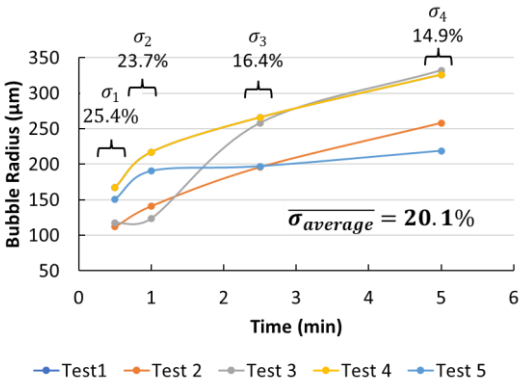

Figure 4: Bubble size control testing of the transient bubble growth over 5 minutes to observe the average deviation overtime.

Electromagnetic Flow for Rapid Bubble Transportation

The measurements showed that magnetic-field-assisted transportation period of a bubble from the nucleation site to the capacitive sensing site reduced from 15 min to 5 min to 5 sec as the applied magnetics flux increased from 0 mT to 5 mT to 195 mT, as shown in Fig. 5. The corresponding velocity of the transported bubble were 0.10, 0.26. and 0.44

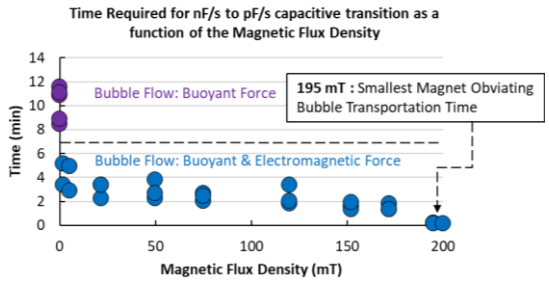

Figure 5: Experimental data of the time required to produce sufficient bubble for analyses at the capacitive sensor as a function of the magnetic flux density while minimizing the magnet size.

$mm \cdot s^{-1}$, respectively. At the optimal point, a minimum magnetic field strength of 195 mT was selected, enabling near real-time transportation of the bubble and decreasing the sensor's previous response time from 15 minutes to 5 minutes. This is crucial, as measurements must occur every 10-60 minutes to accurately assess changes in CO_2 fluctuation in water [4]

Capacitive CO_2 Concentration Measurements

Initial measurements showed that the average bubble radius increased from 108 µm to 511 µm while the capacitance decreased from 33.6 nF to 1.1 nF, as anticipated, with the increasing dissolved CO_2 concentrations ranging from 0.62 ppm to 987.36 ppm, as shown in Fig.6-a.

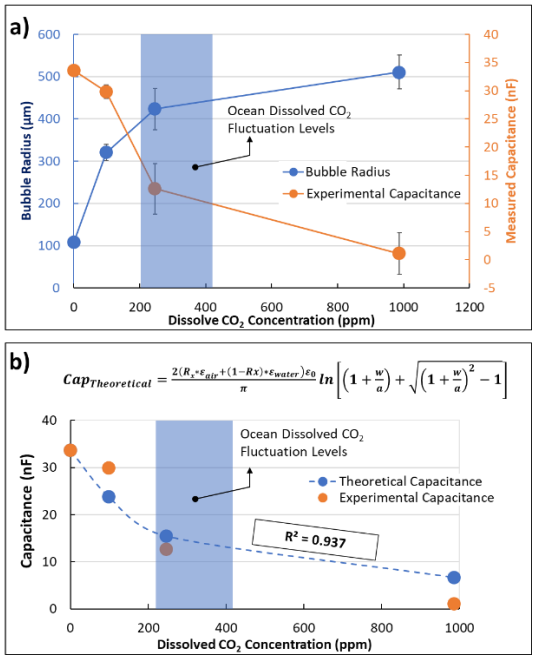

Figure 6: a) Graph of the average bubble radius and average measured capacitance as a function of the CO_2 concentration. b) Graph of the experimental and theoretical capacitance in relation to the CO_2 concentration.

Thus, confirming the expected inverse relationship between dissolved CO_2 concentration and average capacitive measurements, as depicted in Fig. 6b. Experimental average capacitance not only aligned with this anticipated relationship but also displayed a strong correlation to the theoretical capacitance derived from the measured bubble radius ($R^2 = 0.937$), with deviations of ±3 nF. Although a deviation of ±3 nF may seem relatively high, it is primarily attributed to variations in the reference bubble size within the sensor system, which will be addressed in future iterations by employing a trench-based design.

CONCLUSION

This paper validates the feasibility of measuring the bubble size, a parameter closely tied to the dissolved CO_2 concentrations, by integrating a capacitive sensor and establishing a strong correlation between the measured CO_2 concentrations, yielding a coefficient of determination of 0.937. To ensure stable measurements, control over bubble nucleation location and size was achieved through the incorporation of a microcavity and a passivation layer Additionally, an electromagnetic flow was introduced to expedite measurements, successfully reducing the measurement time to 5 seconds. Ultimately, the fabricated prototype effectively correlates bubble sizes to dissolve CO_2 concentrations within the range of 0.62 to 97.36 ppm, thus presenting a promising avenue for measuring dissolved CO_2 concentrations in the ocean with a small form factor and low power consumption, while maintaining stability over time.

ACKNOWLEDGEMENTS

This research work was generously supported by the cooperative agreement of DE-AR0001836 of the ARPAE program (Program Manager: Dr. Simon Freeman). The microfabrication was performed in the Utah Nanofabrication Facility in the University of Utah.

REFERENCES

[1] IPCC, 2022: Climate Change 2022: Impacts, Adaptation and Vulnerability. Contribution of Working Group II to the Sixth Assessment Report of the Intergovernmental Panel on Climate Change Cambridge University Press. Cambridge University Press, Cambridge, UK and New York, NY, USA, 3056 pp.

[2] Friedlingstein, P., O'sullivan, M., Jones, M.W.,Andrew, R.M., Hauck, J., Olsen, A., Peters, G.P., Peters, W., Pongratz, J., Sitch, S., et al. (2020). Global carbon budget 2020. Earth Syst. Sci. Data 12, 3269–3340.

[3] Tran, S., Noh, S. & Kim, K. (2023). Low-Power CO2 Gas Sensor Based on Electrolysis-Induced Bubbles. Transducers 2023, The 22nd International Conference on Solid-State Sensors, Actuators and Microsystems, Kyoto, Japan. Published, 06/2023.

[4] Van der Linde, P., Peñas-López, P., Moreno Soto, Á., van der Meer, D., Lohse, D., Gardeniers, H. J. G. E., & Fernandez Rivas, D. (2019). Gas bubble evolution on microstructured silicon substrates. Energy & Environmental Science.

[5] Yang M, Bell TG, Bidlot J-R, Blomquist BW, Butterworth BJ, Dong Y, Fairall CW, Landwehr S, Marandino CA, Miller SD, Saltzman ES and Zavarsky A (2022) Global Synthesis of Air-Sea CO2 Transfer Velocity Estimates from Ship-Based Eddy Covariance Measurements. Front. Mar. Sci. 9:826421.